

Biomimetic olfactory chips based on large-scale monolithically integrated nanotube sensor arrays

Received: 1 November 2022

Accepted: 23 November 2023

Published online: 10 January 2024

 Check for updates

Chen Wang ^{1,2,3,8,11}, Zhesi Chen ^{1,2,11}, Chak Lam Jonathan Chan ^{1,2}, Zhu'an Wan ^{1,2}, Wenhao Ye ^{1,2}, Wenyang Tang ^{1,2}, Zichao Ma ^{1,9}, Beitao Ren ^{1,3}, Daquan Zhang ^{1,2,3}, Zhilong Song ^{1,2,10}, Yucheng Ding ^{1,3}, Zhenghao Long ^{1,3}, Swapnadeep Poddar¹, Weiqi Zhang ^{1,2}, Zixi Wan ^{1,2}, Feng Xue ^{1,2}, Suman Ma ^{1,4}, Qingfeng Zhou⁵, Geyu Lu⁸, Kai Liu ⁶ & Zhiyong Fan ^{1,2,3,7} ✉

Human olfactory sensors have a large variety of receptor cells that generate signature responses to various gaseous molecules. Ideally, artificial olfactory sensors should have arrays of diverse sensors. However, it is challenging to monolithically integrate large-scale arrays of different high-performance gas sensors. Here we report biomimetic olfactory chips that integrate nanotube sensor arrays on nanoporous substrates with up to 10,000 individually addressable sensors per chip. The range of sensors is achieved using an engineered material composition gradient. Supported by artificial intelligence, the chips offer a high sensitivity to various gases with excellent distinguishability for mixed gases and 24 distinct odours. We also show that the olfactory chips can be combined with vision sensors on a robot dog to create a system that can identify an object in a blind box.

Artificial olfaction and electronic noses (e-noses) aim to emulate the intricate mechanism of the biological olfactory system to effectively discern complex odorant mixtures. Such systems, which have been under development for decades, are of use in a wide-range array of applications, including food, environmental, medical and industrial process control¹. A range of commercial e-noses have already been developed, including AerNos (<https://www.aernos.com>), Alpha MOS Technologies (<https://www.alpha-mos.com>), Sensigent (<https://www.Sensigent.com>), Aryballe Technologies

(<https://aryballe.com>) and Cyrano Sciences (<https://cyranosciences.com>). However, existing e-nose systems still fall short of their biological counterparts^{2–8}.

In practical applications, the primary challenges include the difficulty in miniaturizing the system and poor recognition capabilities in determining the exact gas species and their concentrations within complex odorant mixtures (as opposed to single-gas species). Addressing these deficiencies of e-nose systems is important for existing applications but could also be of use in intelligent systems, such as

¹Department of Electronic and Computer Engineering, The Hong Kong University of Science and Technology, Clear Water Bay, Hong Kong, China. ²The Hong Kong University of Science and Technology–Shenzhen Research Institute, Shenzhen, China. ³State Key Laboratory of Advanced Displays and Optoelectronics Technologies, The Hong Kong University of Science and Technology, Clear Water Bay, Hong Kong, China. ⁴Department of Materials Science and Engineering, Southern University of Science and Technology, Shenzhen, China. ⁵Ai-Sensing Technology Co. Ltd., Foshan National Torch Innovation Pioneering Park, Foshan, China. ⁶State Key Laboratory of New Ceramics and Fine Processing, School of Materials Science and Engineering, Tsinghua University, Beijing, China. ⁷Department of Chemical and Biological Engineering, The Hong Kong University of Science and Technology, Clear Water Bay, Hong Kong, China. ⁸Present address: State Key Laboratory on Integrated Optoelectronics, College of Electronic Science and Engineering, Jilin University, Changchun, China. ⁹Present address: School of Microelectronics, South China University of Technology, Guangzhou, China.

¹⁰Present address: Institute for Energy Research, Jiangsu University, Zhenjiang, China. ¹¹These authors contributed equally: Chen Wang, Zhesi Chen.

✉ e-mail: eezfan@ust.hk

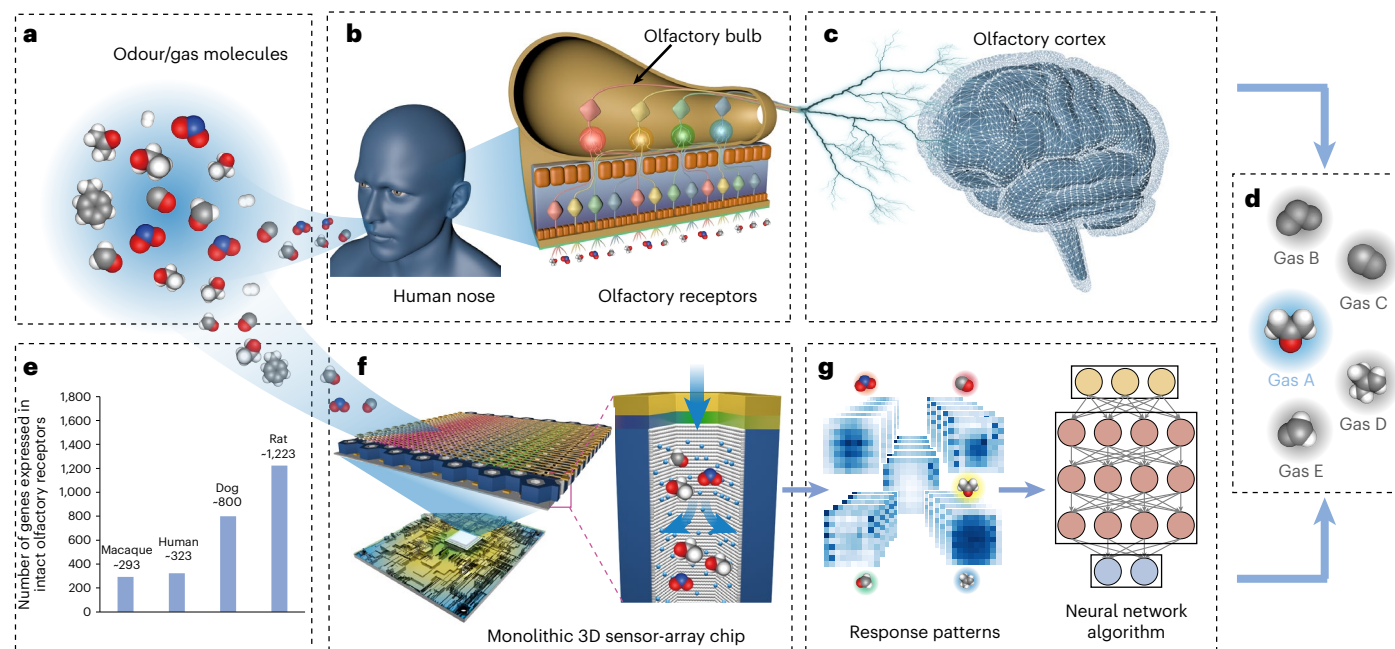


Fig. 1 | Comparison of the mammalian olfactory system and a BOC system.

a, Illustration of odour/gas molecules. **b**, Schematic of the human olfactory system consisting of the olfactory epithelium and the olfactory bulb. **c**, Structure of the olfactory cortex. **d**, Illustration of the recognition result. **e**, Summary of the numbers of genes expressed in intact olfactory receptors from different

mammals: macaque, human, dog and rat. **f**, Structure of a monolithic BOC with the correlated circuit. **g**, Response patterns for different odour/gas molecules from the monolithic BOC and the algorithm design for recognizing the response patterns.

advanced robots and portable smart devices, that have applications in, for examples, security patrols and rescue operations.

Mammals can detect and differentiate millions of odours. This occurs through a distinctive encoding-combination strategy employed by the olfactory receptors and neural networks within the brain^{9–11}. The olfactory system in humans (Fig. 1a–d) detects odour/gas molecules that dissolve in the mucus on the olfactory epithelium. These molecules bind to different olfactory receptors on the cilia of olfactory neurons, instigating an electrical response. This response is transmitted through the olfactory nerves and fibres to the olfactory bulbs for processing. Signals are then transmitted by the olfactory bulbs to the olfactory cortex for comprehensive processing that discriminates the odours. Having more types of odour receptor means having a more powerful sense of smell. Canines have, for instance, about 1,000 types of olfactory receptors, making their olfaction superior to that of primates (Fig. 1e)¹².

A smart chemical-sensing unit—the key component that determines the performance of an e-nose system—is predominantly a gas sensor array with a variety of discrete gas sensors or a monolithically integrated chip^{1,13,14}. Compared to biological olfactory systems, these small sensor arrays have a restricted range of ‘olfactory receptors’, which limits system performance. Mainstream gas sensors, regardless of their physical or chemical working principle (which include metal oxide (MOX) sensors, polymer sensors, surface acoustic wave sensors, quartz crystal microbalance sensors, electrochemical sensors and nondispersive infrared sensors), are typically individual sensors with large form factors^{15–20}. Many of the devices are power hungry and have poor selectivity; some are also characterized by a narrow selection band (electrochemical and nondispersive infrared sensors) and can detect only a single type of gas (Supplementary Table 1). These sensors are designed for specific applications, and hence their performance is not optimal for generic tasks.

State-of-the-art microelectromechanical systems (MEMS) have enabled the monolithic integration of millions of identical sensors, but creating a diversity of sensors beyond hundreds on a single chip

is difficult^{21–24}. The methodologies explored to construct diversified sensor arrays are relatively primitive. These methods primarily involve drop-coating, printing, chemical vapour deposition or physical vapour deposition of different sensing materials (such as polymers, MOXs and functionalized carbon nanotubes) sequentially^{13,21–26}. Sensing films produced by drop-coating or printing methods often exhibit poor mechanical strength, whereas sensing films generated by chemical vapour deposition or physical vapour deposition tend to have inferior sensing performance because of the small surface area-to-volume ratio in the dense sensing film^{13,26}.

Attempts have been made to tackle these issues by employing techniques such as glancing angle deposition to create nano-rod nanostructures with enhanced sensing properties. However, ensuring consistent reproducibility for mass production remains challenging²⁷. Moreover, it is difficult to create hundreds of different types of gas-sensing materials, regardless of whether organic or inorganic materials are used, and most sensors use similar materials with different dopants. Efforts have been made to develop chips based on a large sensor array with a temperature gradient and a gradient of overlapping membrane layers (the Kamina electronic nose)²⁶. However, despite their intriguing design, these devices have not attained commercial success. The key challenges associated with such devices are their high power consumption and limited diversity¹⁴. Furthermore, the current algorithms used in e-nose systems are relatively singular and difficult to adapt to different applications²⁸.

In this Article, we report biomimetic olfactory chips (BOCs) based on large monolithically integrated sensor arrays (Fig. 1f,g). Each BOC comprises a high-density array of vertical MOX nanotubes with a well-defined three-dimensional (3D) nanostructure and a range of pixel types. It is supported by a peripheral signal read-out circuit and advanced neural network algorithms. The number of sensors in a BOC ranges from 100 to 10,000 to mimic the diversity of biological olfactory receptors. The monolithic 3D chemical sensor-array chip was fabricated using atomic layer deposition (ALD) of MOX and subsequent

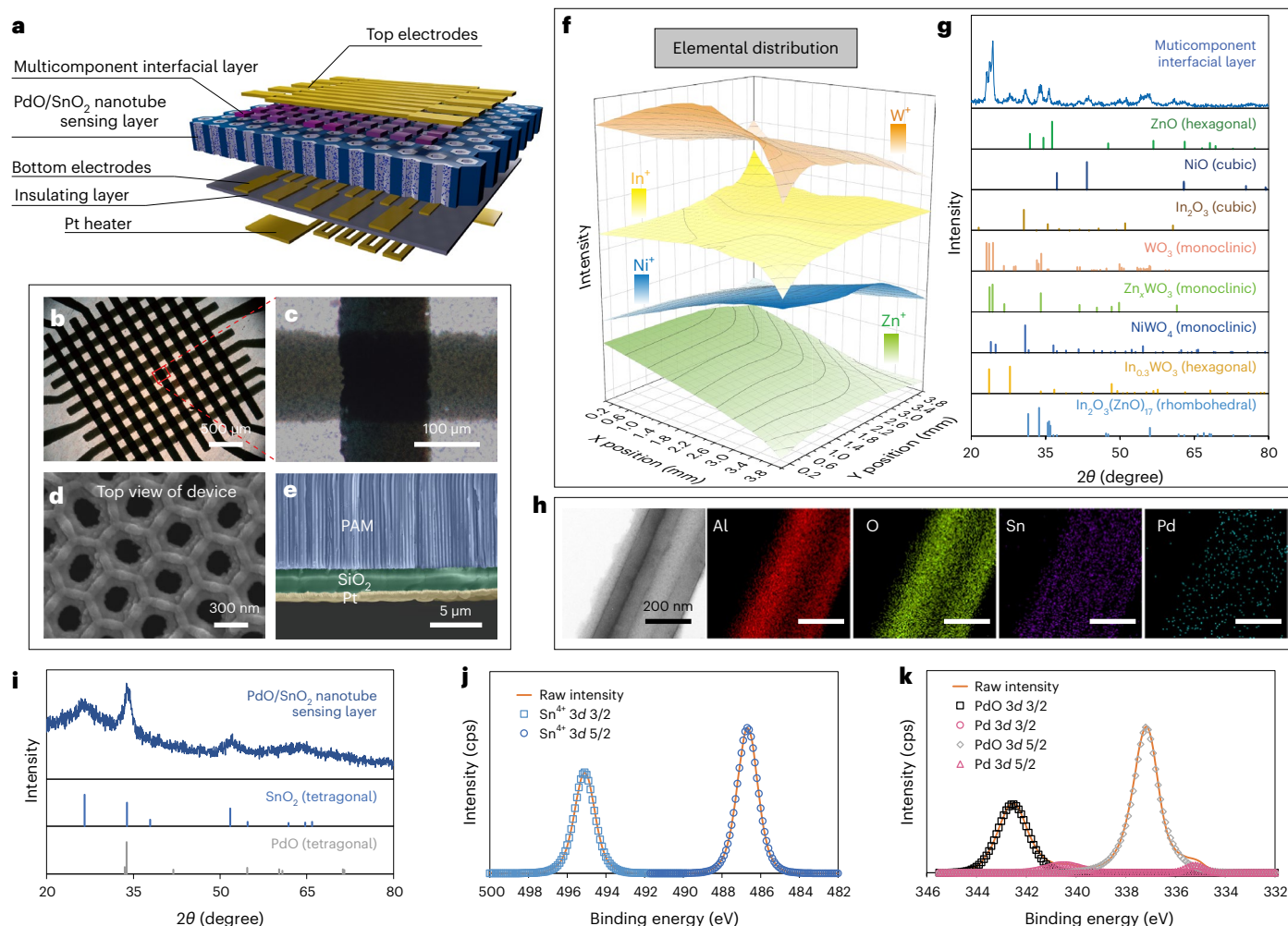


Fig. 2 | Structural analysis of the BOC device. a, Schematic of the monolithic BOC. **b**, Optical image of the top view of the BOC. **c**, Optical image of a single pixel in the BOC. **d**, SEM image of the top view of the BOC. **e**, SEM image of a cross section of the BOC. The different colours indicate the different components (bottom region). **f**, Spatial distribution of elements in the MCI layer visualized

using the loci of ToF-SIMS depth profiles. **g**, XRD pattern of the MCI layer. **h**, TEM and EDS mapping of a single channel of the PdO/SnO₂/PAM. **i**, XRD pattern of the sensing-material layer (PdO/SnO₂). **j,k**, High-resolution XPS spectra of Sn 3d (**j**) and Pd 3d (**k**) of the sensing-material layer (PdO/SnO₂). cps, counts per second.

suspended mask-assisted sputtering (SMAS) of diverse MOX. A vertical sensor structure with a precisely controlled nanoscale sensing-material layer was constructed on nanotubular porous alumina membrane (PAM), enabling excellent detection sensitivity to ppb-level concentrations of a molecular gas. The SMAS method forms a multi-component interfacial (MCI) layer with a gradient distribution of MOX elements on the free-standing PAM, which plays a key role in creating the range of sensors. The vertical device structure allows the use of top-to-bottom crossbar electrodes to maximize the number of pixels in the miniaturized structure.

We fabricated a 100 × 100 sensor array with individual sensors of size 10 × 10 μm². We also examined different scales of integration, including 10 × 10 and 20 × 20 sensors. The pixel diversity of the BOC was used to generate a set of signature patterns for different gas or odour molecules (Fig. 1g). Using neural network algorithms, the BOC can recognize eight gas species at various concentrations in different humidity backgrounds with a prediction accuracy of up to 99.04%. The system can accurately recognize the components and concentrations of gas mixtures and can recognize 24 typical odours. To illustrate the potential of our approach, we installed a BOC into a quadrupedal mobile robot (a robot dog), thus allowing it to identify the odour in a blind box.

BOC device fabrication

Figure 2a is a schematic illustration of the structure of our BOC device. It was designed for high-performance gas detection and reliable discrimination. The chip comprises five major components: an MCI layer on top of the PAM substrate, a PdO/SnO₂ nanotube sensing-material layer in the PAM channel, the top and bottom sensing electrodes, an insulating layer and a Pt heater. The fabrication method for the device is not CMOS compatible (Extended Data Fig. 1). Figure 2b shows a 10 × 10 sensor array with a crossbar electrode configuration. The size of the individual sensors depends on the intersection area of the top and bottom electrodes, which is 140 × 140 μm² (Fig. 2c). Thus, 100 sensors encompass an area of about 8 mm². In the magnified scanning electron microscopy (SEM) top-view image (Fig. 2d), the characteristics of the honeycomb-like structure are clear. The diameter of the pores is about 300 nm. Thus, it has a large surface-to-volume ratio, which facilitates the access of gas molecules and the interaction between the gas molecules and the sensing material to give excellent sensing performance^{29–31}. The cross-sectional view of the bottom region of the chip (Fig. 2e and Supplementary Fig. 1) clearly shows the vertical and ordered nanotube structure. A dense insulating SiO₂ layer with a thickness of approximately 2.5 μm delivers excellent electrical insulation between the signal electrode and the underlying Pt heating electrode.

The incorporation of a Pt heater is imperative for elevating the temperature of the 3D sensor-array chip to achieve optimal sensitivity.

The manufacturing process utilized in our study boasts a distinctive advantage of producing pixels with a wide range of responses within a single 3D sensor-array chip. This was achieved by using multi-step SMAS to construct an MCI layer, which effectively governs the transport of carriers between the top electrode and the sensing-material layer. This multi-step SMAS method created a two-dimensional (2D) MOX composition gradient in the MCI layer (Supplementary Figs. 2–4). By tuning the distance between the suspended mask and the PAM substrate and also the relative position of the mask on the PAM, four different MOXs (ZnO , NiO , In_2O_3 and WO_3) were successively deposited onto the PAM surface after the ALD of the Pd/SnO_2 nanotube sensing-material layer (Supplementary Text 1). The spatial distribution of elements in the MCI layer was measured using time-of-flight secondary ion mass spectrometry (ToF-SIMS). The SIMS depth profiles were acquired in 16 regions with a 4×4 array, and the data were used to calculate the ion concentrations (Supplementary Figs. 5–7). Each of the four cations (Zn^+ , Ni^+ , In^+ and W^+) has a gradient distribution along the four orthogonal directions in 2D space; thus, they constitute different pixels in the MCI layer (Fig. 2f and Supplementary Figs. 8 and 9). The crystalline phases of the MCI layer were verified by X-ray diffraction (XRD) (Fig. 2g). New compounds, including Zn_xWO_3 (monoclinic, JCPDS no. 43-1035), NiWO_4 (monoclinic, JCPDS no. 51-225), $\text{In}_{2.2}\text{WO}_3$ (hexagonal, JCPDS no. 37-30) and $\text{In}_2\text{O}_3(\text{ZnO})_{17}$ (rhombohedral, JCPDS no. 43-621), were formed during postannealing at 450 °C in addition to the original four oxides (Supplementary Fig. 10).

The sensing-material layer in the PAM channels has a key role in determining the final performance of the 3D sensor-array chip (Supplementary Text 1). ALD was employed to achieve the uniform deposition of materials in the PAM channels³⁰. SnO_2 and Pd layers were successively deposited and annealed at 450 °C to improve their crystallinity. The uniformity of the thin film was verified by the uniform distribution of elemental Sn and Pd in a single PAM channel, as shown in transmission electron microscopy (TEM) and energy-dispersive X-ray spectroscopy (EDS) mapping (Fig. 2h). The crystal structure and composition of the sensing-material layer were determined by XRD, X-ray photoelectron spectroscopy (XPS) and high-resolution scanning TEM. From these analyses, the tetragonal structures of SnO_2 (JCPDS no. 41-1445) and PdO (JCPDS no. 41-1107) were confirmed, which ultimately formed the PdO/SnO_2 heterojunction sensing-material layer (Fig. 2i–k and Supplementary Figs. 11 and 12).

Device measurement and consistency validation

The peripheral read-out circuit in the BOC was designed to solve the sneaky path issue that is induced by the crossbar structure of the electrodes (Fig. 3a and Supplementary Figs. 13 and 14)³². The resistance of each pixel in the monolithic 3D sensor-array chip can be read out accurately (Supplementary Fig. 15). To verify the functionality of our BOC, a 10×10 sensor-array chip was chosen as a proof of concept. The chip was suspended and bonded onto a dual in-line ceramic package to give a good electrical contact and good heat dissipation. For the working temperature of 175 °C used in this work, the power consumption was about 240 mW (Supplementary Fig. 16). Each pixel responded differently to different gases, which are reflected in the resistance and gas response. The resistances of the 10×10 sensor-array chip in dry air at 175 °C (Fig. 3b and Supplementary Fig. 17) vary in the mega-ohm range with a coefficient of variation (CV) of 48.79%. The statistical distribution of the resistances of pure SnO_2 (CV = 7.12%) and PdO/SnO_2 (CV = 7.98%) sensor-array chips without the MCI layer was also evaluated to assess the availability of the MCI layer.

To substantiate the consistency of our manufacturing process, twelve 100-pixel BOCs were prepared and tested. We, thus, investigated the device-to-device repeatability. Ten sensors at fixed positions, namely the diagonal sensors in the arrays (sensors 1, 12, 23, 34, 45, 56,

67, 78, 89 and 100), were selected. For each sensor from the 12 BOCs, we calculated the average value, standard deviation and CV for the resistance and gas response. The maximum CVs for the resistance and gas response were 17.7% and 17.6%, respectively, demonstrating the comparatively excellent repeatability (Extended Data Fig. 2, Supplementary Fig. 18, and Supplementary Tables 2 and 3).

To examine the perception of our BOC to chemical molecules, eight gas species (acetone, carbon monoxide, ethanol, formaldehyde, nitrogen dioxide, toluene, hydrogen and isobutylene) with concentrations ranging from 20 ppb to 4 ppm were tested. We employed the Pearson correlation matrix to evaluate the degree of linear correlation amongst data points to quantitatively elucidate the interrelation of pixels in the sensor-array chip (Supplementary Fig. 19). The result illustrates that there was a discernible correlation between adjacent pixels in the sensor-array chip. Furthermore, a gradual increase in diversity can be observed with increasing distance from the initial pixel, thereby validating the overall diversity of the entire sensor-array chip in alignment with the gradient material composition design of our BOC.

The dynamic sensing response of ten sensing pixels along the diagonal line of the BOC (Fig. 3a) to 1 ppm to 100 ppb acetone is shown in Fig. 3c, which indicates the reliability of the gas responses and the variable sensing behaviours of the different pixels. Indeed, some sensors have a drifting baseline and relatively long response/recovery times, mainly due to the relatively low working temperature (175 °C). Commercial MOX sensors are usually operated at 300–400 °C to achieve good gas response and baseline stability. Although our BOC was operated at 175 °C, it has an excellent response to ppb-level gas concentrations (Supplementary Table 4). To validate the effect of working temperature on sensing properties, we systematically tested the BOC at different temperatures, namely, 125, 175 and 250 °C (Extended Data Fig. 3 and Supplementary Fig. 20). The response/recovery times gradually decreased with an increase of the working temperature. The gas response reached a maximum at 175 °C. After a comprehensive consideration of these parameters, particularly the response/recovery time, gas response and power consumption, 175 °C was chosen as the optimal working temperature for our BOC.

To visualize the features of the entire BOC, the response values were normalized to a greyscale between 0 and 255 by choosing the responses to 5 ppm H_2 as the ceiling value. The results are presented as heat maps, which show the response patterns for different concentrations of gas species under various humidity conditions (Fig. 3d and Supplementary Figs. 21–37). For a certain gas molecule, the normalized response patterns were highly consistent over a range of concentrations and humidity levels, so that we could recognize the gas species accurately and efficiently (Supplementary Fig. 38). Furthermore, artificial intelligence algorithms were developed to support the BOC by processing the response patterns.

Single-gas discrimination with the BOC system

The BOC that we developed in conjunction with the algorithm constitutes a biomimetic olfactory system. It is a promising tool for mimicking the function of mammalian olfaction. We employed an end-to-end convolutional neural network (CNN) to classify the gas from the response patterns (Fig. 3e and Supplementary Text 2)^{2,33,34}. The actual and predicted gases are shown in the confusion matrix in Fig. 3f, which demonstrates the high prediction accuracy of our model. We then analysed the misclassified data. A misclassification originates mainly from the low concentrations of gas species with similar functional groups, such as acetone and formaldehyde. Encouragingly, for the entire dataset (4,160 samples) of eight gases with different concentrations and humidity levels, the optimized model reached a prediction accuracy of 99.04% and saturated after 500 training epochs. The training loss (testing loss) dropped from the initial 1.32% (1.80%) to 0.02% (0.03%), confirming the robustness and reliability of the end-to-end CNN model utilized for classifying gas response patterns (Fig. 3g).

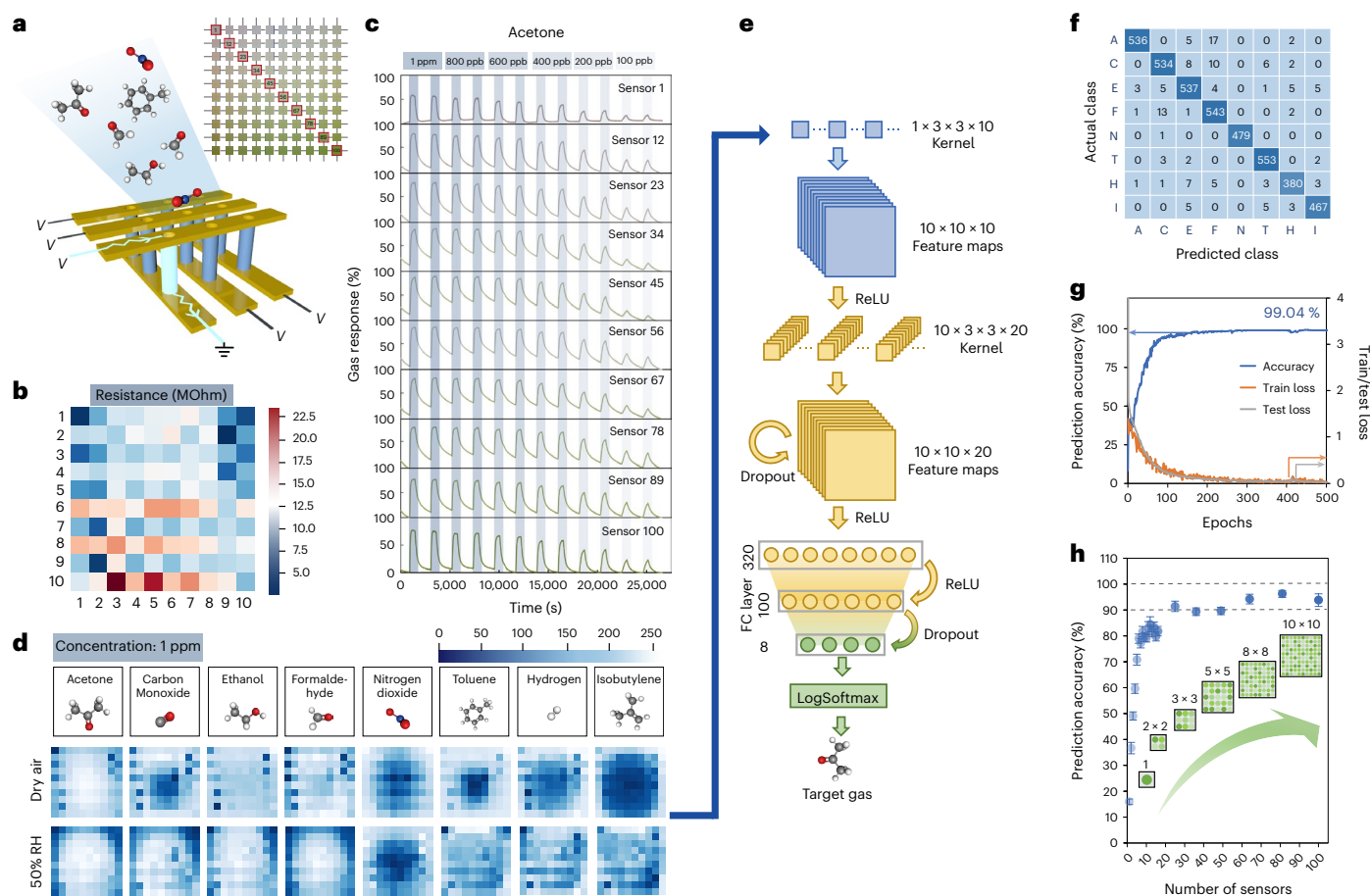


Fig. 3 | Single-gas classification with the BOC. a, Schematic of the crossbar electrodes of the BOC. **b**, Heat map of the resistances of the 10×10 sensor-array chip under dry air at 175°C . **c**, Dynamic sensing curves for ten sensors along the diagonal line of the 10×10 sensor-array chip for acetone at 1 ppm to 100 ppb under dry air as the background gas at 175°C . **d**, Normalized response patterns (greyscale from 0 to 255) for 1 ppm of different gas species under dry air and 50% relative humidity (RH) air as the background gas at 175°C . **e**, Schematic of the CNN for gas classification. **f**, Confusion matrix of the actual class and predicted

class when recognizing eight gases (A, acetone; C, carbon monoxide; E, ethanol; F, formaldehyde; N, nitrogen dioxide; T, toluene; H, hydrogen; I, isobutylene). **g**, Curves for predicted accuracy, training loss and testing loss versus epochs when recognizing eight kinds of gas. **h**, Prediction accuracy versus the number of sensors. The accuracy increases with more sensors. The error bars indicate the standard deviation (s.d.). Data are presented as mean values \pm s.d. FC, fully connected; ReLU, rectified linear unit.

To further prove the robustness of the system, we separated the training and testing data by the time of collection. We kept testing the BOC chip for three months. The sensing data in the first month were used as the training dataset, and sensing data from the second and third months were used as testing datasets (Supplementary Figs. 39–41). The prediction accuracies in the second and third months were 98.55% and 96.67%, respectively (Extended Data Fig. 4). Although a small degradation of performance was observed during this long-term test, the prediction accuracy was still sufficient to satisfy the classification requirements.

Scale of sensor array versus gas classification accuracy

We designed and conducted experiments on accuracy versus the scale of the sensor array to illustrate that increasing the variety of sensors plays an instrumental role in achieving higher accuracy. To guarantee that the chosen sensors sufficiently embody the material composition and discrimination functions of the entire chip, we used sensors evenly distributed throughout the chip (Supplementary Text 2). The dataset used for analysis comprised 4,160 samples. A prediction accuracy of approximately 80% was achieved using only four sensors (Supplementary Fig. 42). However, the limited dataset consisted of only eight

gas species with various concentrations and humidity levels, which accounted for the observed prediction accuracy.

To address this limitation, the remaining ~20% of the data that could not be classified by the four sensors were used as a new dataset for analysis. To ensure a fair comparison of the accuracy versus number of sensor tests, the size of the CNN model and the method for dividing the data were fixed (Supplementary Text 2 and Supplementary Fig. 43). Gases with different humidity levels were considered as different species in this model, resulting in a total of 37 species. Figure 3h shows that the accuracy improved rapidly from 15.98% (single sensor) to 93.83% (100 sensors) as the number of sensors used for classification increased, although the accuracy became saturated after the number of sensors exceeded 25. If the scenario were more complicated with more gas species and larger concentration ranges, the number of sensing pixels needed to reach saturation would be higher. Overall, using more sensors will certainly yield higher accuracy, which could be extended as a generic method to improve the accuracy and reliability of sensor-array systems. Of course, if the number and diversity of pixels (where diversity refers to the receptor types) were increased, the more complicated reading out of the signal and data redundancy would have to be taken into account.

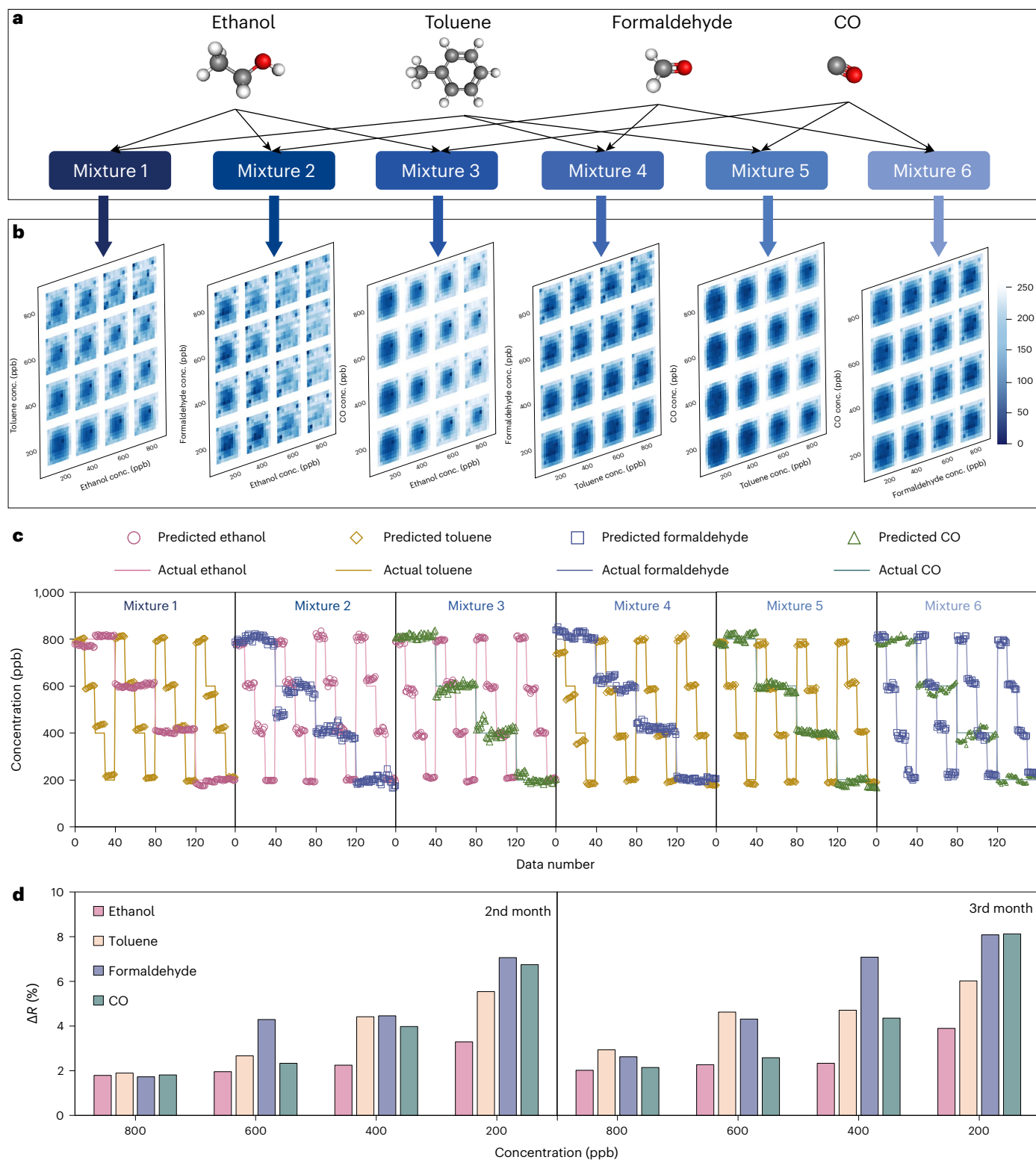


Fig. 4 | Classification of gas mixtures by the BOC. **a**, Experimental design of gas mixtures. **b**, Normalized response patterns for the mixtures with different concentrations of gases. **c**, Concentrations of gas mixtures predicted by a fully connected neural network using the first month's sensing data as the training

dataset and the second month's sensing data as the testing dataset. Data number refers to the number of data we used for algorithm processing. **d**, Average relative error between predicted concentrations and actual concentrations. conc., concentration.

Deconvolution of a gas mixture with the BOC system

Biological olfactory systems can struggle to identify the composition and concentration of various gas mixtures. To tackle this challenge and

demonstrate the capability of our BOC, we conducted a quantitative analysis of gas mixtures with two of four typical gases (ethanol, toluene, formaldehyde and carbon monoxide) in different ratios (Fig. 4a). The dataset included 96 kinds of mixtures with concentrations ranging

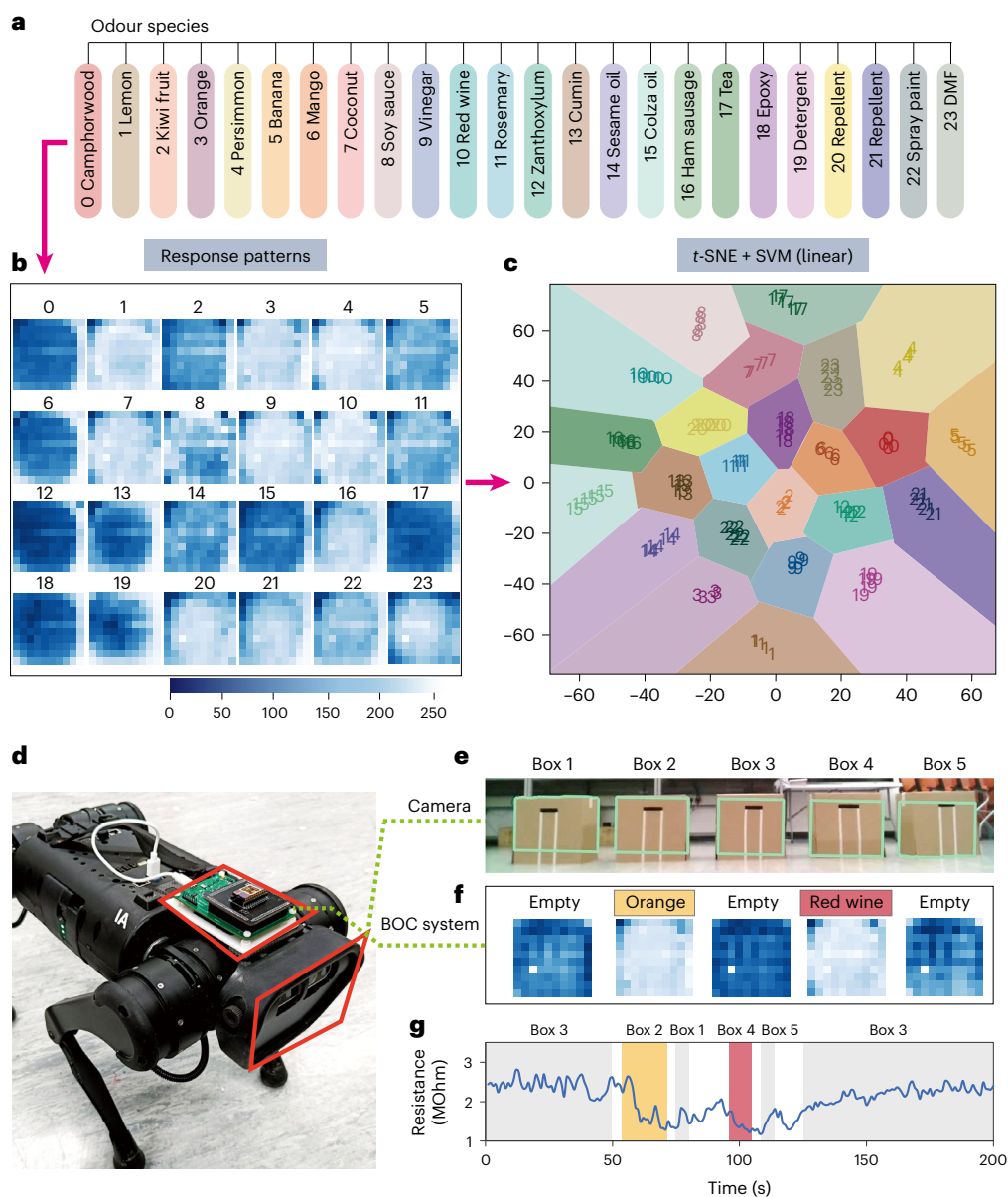


Fig. 5 | Odour classification with the BOC and fusion of olfactory and vision sensors in a robot. a, Odour species chosen for recognition by a BOC with 100 sensors. DMF, dimethylformamide. **b**, Normalized response patterns to the 24 odours in **a**. **c**, Classification of 24 odours by *t*-distributed stochastic neighbour embedding (*t*-SNE) and a support vector machine (SVM) with linear kernel

algorithms. **d**, Configuration of the BOC system installed on a quadruped robot for blind box differentiation. **e**, Recognition of boxes by computer vision, that is, the camera. **f**, Recognition result of our BOC system. **g**, Real-time recorded resistance signal of sensor 61.

from 200 to 800 ppb. As illustrated in Fig. 4b, the response patterns changed smoothly with increasing concentration. Taking the mixture of toluene and ethanol as an example, with an increase in the concentration of ethanol, the edge regions of the response patterns gradually became brighter, which is the same as when the two gases are present separately. However, since the response of the sensors to the mixture is not simply the sum of two responses from the separate gases due to the competitive adsorption and cross-reactions on the surface of the sensing material, the different response patterns make it possible for an algorithmic model to distinguish the components and concentrations of the mixture.

As in the single-gas species tests, we separated the training and testing data by time of collection to determine the robustness of the system in a quantitative analysis of gas mixtures (Supplementary Figs. 44–47). The CNN that we utilized before is proficient in feature

extraction. However, when applied to regression, such as predicting gas concentrations, the parameterization is time-consuming and computationally intensive. Here, instead of feeding all the raw data into the neural network model, which is complicated and time-consuming, the gas response patterns were first dimensionally reduced to ten-dimensional vectors by principal component analysis, which both reduced the noise and improved the performance of the model. Subsequently, a five-layer fully connected neural network was trained end to end to predict the concentrations of two-gas mixtures. The model has four output neurons to represent the concentrations of ethanol, toluene, formaldehyde and carbon monoxide.

Figure 4c illustrates the predicted concentrations using the first month's sensing data as the training dataset and the second month's sensing data as the testing dataset (results for the third month's sensing data are shown in Supplementary Fig. 48). The results of a statistical

analysis of the predicted concentrations are shown in Fig. 4d. The average relative error between the predicted concentration and the actual concentration of mixtures was calculated as follows:

$$\Delta R = \frac{\text{Mean}(\text{Abs}(\text{Pre}_{\text{gas } N} - \text{Act}_{\text{gas } N}))}{\text{Act}_{\text{gas } N}} \times 100\%, \quad (1)$$

where $\text{Pre}_{\text{gas } N}$ is the average of the predicted concentrations of gas N and $\text{Act}_{\text{gas } N}$ is the actual concentration of gas N . Here N represents ethanol, toluene, formaldehyde or carbon monoxide. The maximum ΔR increased from 7.05% to 8.12% for 200 ppb of a gas species between the data for the second and third months. For the highest concentration (800 ppb), ΔR was lower than 3%, which proves the accuracy and reliability of our BOC for gas-mixture recognition.

Real-time odour classification with the BOC system

We are surrounded by various types of odours, each odour of which may have a complex gas composition. The identification and perception of odours can not only regulate our emotions, but also sometimes is a matter of life and death. To demonstrate the capability of our BOC system to classify odours, we selected 24 objects with different odours, as listed in Fig. 5a. One hundred gas response patterns for each odour were collected after the signal had stabilized (Fig. 5b and Supplementary Fig. 49). To view the distribution and relationship of the 24 odours tested by the BOC system, we employed t -distributed stochastic neighbour embedding to convert the 100-dimensional Euclidean distance into 2D coordinates using the 30 nearest neighbours among the whole dataset according to the conditional probability³⁵. Furthermore, we adopted a support vector machine algorithm with a linear kernel to divide up the decision space. Each odour is represented by one number and one colour (Fig. 5c and Supplementary Fig. 50). As a result, all 24 odours are distributed in the space. A real-time demonstration of the BOC system identifying a quantity of red wine and a piece of an orange is shown in Supplementary Video 1. The result substantiates the excellent classification capability of our BOC system. In addition, the capability of our BOC system to identify the freshness or safety of food is also validated with a time-dependent test of a sliced orange (Supplementary Figs. 51 and 52).

Fusion of olfactory and vision sensors on a robot

Elevating intelligence is an inevitable trend in the development of advanced robotics. Sensor technology is one of the foundations of a robotic implementation. Multi-sensor fusion combines information from different sensors to provide a more accurate and reliable perception of the external environment, thus improving the rationality of robot decision-making. Even though researchers have integrated many different types of sensors on robots, such as temperature sensors, tactile sensors, sound sensors and various kinds of light sensors, olfactory sensors have rarely been used. In fact, equipping a robot with a sense of smell can make it much more intelligent and expand its range of applications.

To demonstrate the potency of our BOC system for advanced robotics, as shown in Fig. 5d, a BOC system was installed on a robot dog to bestow the olfactory function on the robot (Supplementary Text 3). To examine the functionality of the robot, five similar boxes were placed in a line. Two of them contained objects with different odours (a sample of red wine or a piece of an orange) (Extended Data Fig. 5). It is impossible to identify the content of these boxes with only vision sensors (cameras) (Fig. 5e). However, with an olfactory function (BOC system), the robot first recognizes the shape of a box with its vision. It moves from box to box and can identify the internal objects (red wine, a piece of orange or empty) utilizing its olfaction capability (Fig. 5f and Supplementary Video 2). Figure 5g depicts the real-time signal from a typical sensor (no. 61) from our BOC. In this mini reconnaissance

mission, through the fusion of vision and olfaction, the robot can effectively and accurately identify the objects in blind boxes. This clearly demonstrates the immense potential of robots equipped with olfaction capabilities for a diverse array of future applications, encompassing security, anti-terrorism, disaster relief and beyond.

Construction of large sensor arrays

Expanding the sensor array has the potential to enhance discrimination power. To substantiate the technological feasibility of constructing a large sensor-array chip, we fabricated a 20×20 sensor-array BOC (with 400 sensors) and a 100×100 sensor-array BOC (with 10,000 sensors). Both have a crossbar electrode configuration (Extended Data Fig. 6). The 20×20 sensor-array chip, with an individual sensor size of $100 \times 100 \mu\text{m}^2$, was fabricated by electrode deposition with a shadow mask. Its gas response pattern to 1 ppm acetone was collected to assess its functionality. The 100×100 sensor-array chip was fabricated by photolithography, resulting in individual sensors of size $10 \times 10 \mu\text{m}^2$. The 10,000 sensors occupy an area of about 4 mm^2 . Its gas response patterns to 1 ppm acetone, ethanol, toluene and formaldehyde demonstrate its ultra-high resolution compared to the 10×10 and 20×20 sensor-array chips (Supplementary Fig. 53). With the aid of a more advanced algorithm, this BOC has the potential to be utilized under highly complex gas/odour scenarios.

Conclusions

We have reported a biomimetic olfactory system based on large monolithically integrated nanotube sensor arrays. Our system uses a monolithic 3D MOX sensor-array chip, fabricated on a nanoporous PAM with ALD and a multi-step SMAS method. This produces a MOX MCI layer on top of nanotube sensors. The MCI layer has a 2D material composition gradient, which enables a large diversity of sensing pixels inside the array. Thus, large sensor arrays ranging from 100 pixels to 10,000 pixels can be fabricated.

The sensors have ppb-level sensing performance. With the assistance of different algorithms, the system exhibits high accuracy (up to 99.04%) in classifying several gas species. Moreover, the system offers excellent reliability, accurately identifying the components and concentrations of gas mixtures with a maximum absolute relative error of 8.12% during a three-month testing period. It can distinguish 24 odours. Finally, we integrated a BOC into a quadrupedal mobile robot, so that it combines visual and olfactory senses, which could be used for small reconnaissance missions.

Our BOC devices do have certain limitations. The issues associated with MOX technology—which include a long-term drift of the baseline, relatively high resistance, relatively high power consumption (though lower than other MOX sensors) and a long response/recovery time—necessitate further investigation and improvement. We also note the need to enhance the manufacturing consistency of our sensor chips. Improving device-to-device and batch-to-batch consistency will require further optimization of the fabrication process. Furthermore, the capabilities of the current device may not satisfy the high industrial standard of maintaining a less than 5% variation, so that further improvements are essential.

Methods

Deposition of a PdO/SnO₂ sensing film

The device was built using a custom MEMS fabrication process, which is incompatible with conventional CMOS due to the free-standing PAM (thickness $45 \mu\text{m}$, pixel size 450 nm and pore diameter 300 nm). PAMs were purchased from Shenzhen Top Membranes Technology Co., Ltd. A shadow mask with a 4 mm by 4 mm window size tightly covered the PAM substrate to define the deposition region. An SnO₂ film was grown by ALD (MNT Micro and Nanotech Co., Ltd) on the PAM substrate using tetrakis (dimethylamino) tin ($\text{C}_8\text{H}_{24}\text{N}_4\text{Sn}$, TDMAS, 99.999%) and H_2O as the precursors and N_2 as the carrier and purging gas. The temperatures

of the TDMAS and H₂O were maintained at 70 and 25 °C, respectively. The temperature of reaction chamber was kept at 150 °C. SnO₂ was deposited during 60 cycles of the process. Then Pd was deposited during six cycles, also using ALD. In this procedure, palladium (II) hexafluoroacetylacetonate (99.999%) and hydrazine anhydrous were the precursors at temperatures of 80 and 25 °C, respectively. The chamber temperature was 200 °C. After that, the sample was transferred to the sputtering system for the next step.

Deposition of a suspended mask-assisted gradient film

Supplementary Figs. 2–4 show the process schematically. A mask with a square window measuring 8 mm × 8 mm was suspended over the PAM substrate. Diffraction of the plasma flux at the edge of the mask window leads to the formation of a gradient in the film during sputtering. The mask height was systematically optimized for different materials, as illustrated in Supplementary Figs. 2 and 3. Ultimately, a height of 6 mm was selected to deposit four kinds of MOX in the sequence ZnO, NiO, In₂O₃ and WO₃. Notably, there was a 2 mm shift between the suspended mask window and the mask window on the PAM substrate. To enhance the variation of the distribution of each element, the suspended mask was turned through 90° for the deposition of each MOX. Finally, the sample was annealed at 450 °C for 3 h following the sputtering process.

Fabrication of electrodes, insulating layer and heater

Thermal evaporation was utilized twice to deposit 150 nm of Au on the top and bottom of the sample as the contact electrodes. For the 10 × 10 sensor-array chip, a shadow mask with ten lines (width and gap both 140 μm) was designed to define the electrode pattern. For the 20 × 20 sensor-array chip, the line width and gap of the shadow mask were reduced to 100 μm. For the 100 × 100 sensor-array chip, we used photolithography with two line widths (10 μm and 25 μm), which was performed on a Karl Suss MA6 system with a HPR 506 photoresist, with process conditions being dual coating at 3,000 rpm for an exposure time of 16 s. After the electrode deposition, a 2.5 μm SiO₂ layer was deposited on the bottom side of the sample by electron-beam evaporation as the insulating layer. Finally, a 200 nm serpentine Pt heater was deposited onto the insulating layer by electron-beam evaporation to provide the optimal working temperature for the sensor-array chip. The performance of the Pt heater is characterized in Supplementary Fig. 16.

Material characterization

The XRD patterns were collected by a X'pert Pro diffractometer (PANalytical). The SEM images of the surface and cross sections were captured with the JEOL JSM-7100F and JSM-7800F instruments. The TEM image of the single PAM channel was acquired on a JEOL JEM 2010F instrument. The EDS elemental mapping was obtained by SEM and TEM attachments. The XPS measurements were conducted on a multi-technique surface analysis system (Kratos Axis Ultra DLD Spectrometer). The SIMS depth profiles were acquired by a ToF-SIMS spectrometer (Type V, ION-TOF GmbH). The thickness of the film produced by sputtering was characterized by a surface profiler (Alpha-Step D500 stylus profiler).

Sensing measurements

The sensor-array chips, fabricated using the aforementioned procedure, were bonded to a dual in-line ceramic package or leadless chip carrier using copper wire and silver paste, which ensure reliable electrical contact and a high signal-to-noise ratio. Notably, the sensor-array chip was suspended after the bonding process, resulting in optimal gas transmission capabilities. The packaged chip was integrated with an electrical circuit for reading out the electrical signal. The sensing measurements were performed in a 15 × 15 × 10 cm³ chamber using a dynamic gas flow method with a homemade gas supply system, which comprises a series of mass flow controllers connected to gas cylinders. Supplementary Fig. S4 is a schematic of the gas-sensing system. The carrier gas was synthetic air composed of 20% oxygen and 80% nitrogen.

The testing gases with a fixed concentration (50 ppm/1,000 ppm) were purchased from Asia Pacific Gas Enterprise Co., Ltd. The testing gas concentration was controlled through the dilution method with our own MATLAB programme, which regulates the ratio of the flow rates of the carrier and testing gases. The total flow rate was maintained at 500 sccm. Moreover, the programme can provide different gas pluses with accurate on and off times. The humidity was controlled by the bubbling method with a standard humidity sensor in a testing chamber for calibration. The gas response is defined as $(R_a - R_g)/R_a \times 100\%$ (reducing gases) and $(R_g - R_a)/R_g \times 100\%$ (oxidizing gases), where R_a and R_g are the resistances of sensors exposed to background gases (dry/wet air) and target gases, respectively.

Description of read-out circuit

To acquire signals from our gas sensor array with a crossbar structure, a read-out circuit capable of supporting a 32 × 32 array was designed and fabricated. The detailed design of the electrical circuit is illustrated in Supplementary Figs. 13 and 14. The resistance measurement of a single pixel was based on a voltage divider circuit with a reference resistor. Feedback was applied to idle electrodes to eliminate crosstalk. The active pixel was selected by connecting the corresponding column electrode to the reference resistor through the first multiplexer (MUX1) while its row electrode was grounded through MUX2. For example, to test the resistance of the sensor at row i and column j , MUX1 connected one end of sensor (i, j) to a reference resistor. The other end of sensor (i, j) was grounded by connecting the input of amp _{i} to ground with MUX2. Then sensor (i, j) and the reference resistor form a voltage divider circuit, so that the voltage signal can be tested after buffering. To eliminate crosstalk from adjacent sensors, this circuit ensures that the voltage of the other electrodes in row i and column j remain at V_{out} . This prevented any sneak current flowing between the row i electrode and column j electrode with other electrodes. For the column electrodes, only switch j was open, while the other switches remain closed. As a result, all column electrodes were connected to V_{out} . Similarly, the row electrodes outside of row i were also connected to V_{out} through buffers. This configuration ensures proper isolation and eliminates interference between electrodes. The signal from the voltage divider circuit went through a low-pass filter and was sampled by a 16 bit analogue-to-digital converter (AD7683). The measurement range was 0.02 to 1,000 MΩ, which effectively accommodates the resistances of our devices. A microprogrammed control unit was used to synchronize these MUXs and the analogue-to-digital conversion sampling. For the 10 × 10 sensor array, the test period was 1 s per frame. For the 20 × 20 sensor array, the test period was 4 s per frame. The 100 × 100 sensor-array chip was read out by an assembled system. Specifically, the chip was connected to source measurement units (PXI-4130, National Instruments) through two 128-channel multipixel units (PXI-2530B, National Instruments), which were installed inside a chassis (PXI-1031, National Instruments). The entire system was controlled by a home-built Python program. For the 100 × 100 sensor array, the test period was 45 s per frame.

Data availability

Data that support the findings of the study are available from the corresponding author upon reasonable request. Source data are provided with this paper.

Code availability

All the codes used to support the conclusions of the paper are available from the corresponding author upon reasonable request.

References

1. Persaud, K. & Dodd, G. Analysis of discrimination mechanisms in the mammalian olfactory system using a model nose. *Nature* **299**, 352–355 (1982).

2. Johnson, K. J. & Rose-Pehrsson, S. L. Sensor array design for complex sensing tasks. *Annu. Rev. Anal. Chem.* **8**, 287–310 (2015).
3. Lonergan, M. C. et al. Array-based vapor sensing using chemically sensitive, carbon black-polymer resistors. *Chem. Mater.* **8**, 2298–2312 (1996).
4. Röck, F., Barsan, N. & Weimar, U. Electronic nose: current status and future trends. *Chem. Rev.* **108**, 705–725 (2008).
5. Jeong, S. Y., Kim, J. S. & Lee, J. H. Rational design of semiconductor-based chemiresistors and their libraries for next-generation artificial olfaction. *Adv. Mater.* **32**, 2002075 (2020).
6. Geng, Y., Peveler, W. J. & Rotello, V. M. Array-based ‘chemical nose’ sensing in diagnostics and drug discovery. *Angew. Chem., Int. Ed.* **58**, 5190–5200 (2019).
7. Johnson, K. & Knapp, A. Selectivity measure for arrays of non-specific sensors. *Sens. Actuators B Chem.* **251**, 1076–1088 (2017).
8. Turner, A. P. & Magan, N. Electronic noses and disease diagnostics. *Nat. Rev. Microbiol.* **2**, 160–166 (2004).
9. Buck, L. B. Unraveling the sense of smell (Nobel Lecture). *Angew. Chem., Int. Ed.* **44**, 6128–6140 (2005).
10. Saraiva, L. R. et al. A transcriptomic atlas of mammalian olfactory mucosae reveals an evolutionary influence on food odor detection in humans. *Sci. Adv.* **5**, eaax0396 (2019).
11. Mori, K., Nagao, H. & Yoshihara, Y. The olfactory bulb: coding and processing of odor molecule information. *Science* **286**, 711–715 (1999).
12. Jenkins, E. K., DeChant, M. T. & Perry, E. B. When the nose doesn’t know: canine olfactory function associated with health, management, and potential links to microbiota. *Front. Vet. Sci.* **5**, 56 (2018).
13. Kang, H. et al. Multiarray nanopattern electronic nose (e-nose) by high-resolution top-down nanolithography. *Adv. Funct. Mater.* **30**, 2002486 (2020).
14. Covington, J. A., Marco, S., Persaud, K. C., Schiffman, S. S. & Nagle, H. T. Artificial olfaction in the 21st century. *IEEE Sens. J.* **21**, 12969–12990 (2021).
15. Stetter, J. R. & Li, J. Amperometric gas sensors – a review. *Chem. Rev.* **108**, 352–366 (2008).
16. Dinh, T. V., Choi, I. Y., Son, Y. S. & Kim, J. C. A review on non-dispersive infrared gas sensors: improvement of sensor detection limit and interference correction. *Sens. Actuators B Chem.* **231**, 529–538 (2016).
17. Kumar, A. & Prajesh, R. The potential of acoustic wave devices for gas sensing applications. *Sens. Actuators A Phys.* **339**, 113498 (2022).
18. Liu, X., Zheng, W., Kumar, R., Kumar, M. & Zhang, J. Conducting polymer-based nanostructures for gas sensors. *Coord. Chem. Rev.* **462**, 214517 (2022).
19. Liu, K. & Zhang, C. Volatile organic compounds gas sensor based on quartz crystal microbalance for fruit freshness detection: a review. *Food Chem.* **334**, 127615 (2021).
20. Dey, A. Semiconductor metal oxide gas sensors: a review. *Mater. Sci. Eng. B Solid-State Mater. Adv. Technol.* **229**, 206–217 (2018).
21. Shulaker, M. M. et al. Three-dimensional integration of nanotechnologies for computing and data storage on a single chip. *Nature* **547**, 74–78 (2017).
22. Che Harun, F. K., Taylor, J. E., Covington, J. A. & Gardner, J. W. An electronic nose employing dual-channel odour separation columns with large chemosensor arrays for advanced odour discrimination. *Sens. Actuators B Chem.* **141**, 134–140 (2009).
23. Beccherelli, R., Zampetti, E., Pantalei, S., Bernabei, M. & Persaud, K. C. Design of a very large chemical sensor system for mimicking biological olfaction. *Sens. Actuators B Chem.* **146**, 446–452 (2010).
24. Horrillo, M. C. et al. Measurements of VOCs with a semiconductor electronic nose. *J. Electrochem. Soc.* **145**, 2486 (1998).
25. Kang, K. et al. Micropatterning of metal oxide nanofibers by electrohydrodynamic (EHD) printing towards highly integrated and multiplexed gas sensor applications. *Sens. Actuators B Chem.* **250**, 574–583 (2017).
26. Goschnick, J., Koronczi, I., Frietsch, M. & Kiselev, I. Water pollution recognition with the electronic nose KAMINA. *Sens. Actuators B Chem.* **106**, 182–186 (2005).
27. Moon, H. G. et al. All villi-like metal oxide nanostructures-based chemiresistive electronic nose for an exhaled breath analyzer. *Sens. Actuators B Chem.* **257**, 295–302 (2018).
28. Chen, Z., Chen, Z., Song, Z., Ye, W. & Fan, Z. Smart gas sensor arrays powered by artificial intelligence. *J. Semicond.* **40**, 111601 (2019).
29. Chen, J. et al. Ultra-low-power smart electronic nose system based on three-dimensional tin oxide nanotube arrays. *ACS Nano* **12**, 6079–6088 (2018).
30. Song, Z. et al. Wireless self-powered high-performance integrated nanostructured-gas-sensor network for future smart homes. *ACS Nano* **15**, 7659–7667 (2021).
31. Tang, W. et al. Microheater integrated nanotube array gas sensor for parts-per-trillion level gas detection and single sensor-based gas discrimination. *ACS Nano* **16**, 10968–10978 (2022).
32. Sundaram, S. et al. Learning the signatures of the human grasp using a scalable tactile glove. *Nature* **569**, 698–702 (2019).
33. Lecun, Y., Bengio, Y. & Hinton, G. Deep learning. *Nature* **521**, 436–444 (2015).
34. Albert, K. J. et al. Cross-reactive chemical sensor arrays. *Chem. Rev.* **100**, 2595–2626 (2000).
35. Laurens van der Maaten, G. H. Visualizing data using t-SNE. *J. Mach. Learn. Res.* **9**, 2579–2605 (2008).

Acknowledgements

This work is supported by the National Key Research and Development Program of China (grant no. 2022YFB203500), the Hong Kong Innovation Technology Fund (grant no. GHP/014/19SZ), the Zhongshan Municipal Science and Technology Bureau (grant no. ZSST21EG05), the Internal Fund of the Hong Kong University of Science and Technology (HKUST; grant no. IOPCF21EG01), the Center on Smart Sensors and Environmental Technologies, Foshan HKUST projects (Project Nos. FSUST21-HKUST08D and FSUST21-HKUST09D) and the Foshan Innovative and Entrepreneurial Research Team Program (grant no. 2018IT100031). Z.F. acknowledges support from the New Cornerstone Science Foundation through the XPLOER PRIZE and the Hong Kong Alliance of Technology and Innovation through the Bank of China (Hong Kong) Science and Technology Innovation Prize. We thank the Material and Characterization Preparation Facility and the Nanosystem Fabrication Facility, both at HKUST, and also MNT Micro and Nanotech Co., Ltd for technical assistance.

Author contributions

Z.F., C.W. and Z.C. conceptualized the experiments and methodology design. C.W. fabricated the sensor-array chip and collected the sensing test data. Z.C. designed the algorithm and processed the collected sensing data. W.Y. and C.L.J.C. helped with validating the quadruped robot. Zhu’an Wan and C.L.J.C. assisted with designing and fabricating the read-out circuit. C.L.J.C. and Z.C. designed the interface programme for data acquisition and visualization. W.T., W.Z., B.R., D.Z. and S.M. contributed to the characterization of the materials and devices. Z.M., Z.L., Zixi Wan, F.X., Z.S. and S.P. assisted with the fabrication of the sensor-array chip. Y.D. assisted in designing the figures. G.L. and K.L. contributed to discussions about the paper. Z.F. and Q.Z. provided financial support and oversight of the whole project. C.W., Z.C., Zhu’an Wan and Z.F. wrote the paper. All authors participated in manuscript revision and refinement.

Competing interests

The authors declare no competing interests.

Additional information

Extended data Extended data are available for this paper at <https://doi.org/10.1038/s41928-023-01107-7>.

Supplementary information The online version contains supplementary material available at <https://doi.org/10.1038/s41928-023-01107-7>.

Correspondence and requests for materials should be addressed to Zhiyong Fan.

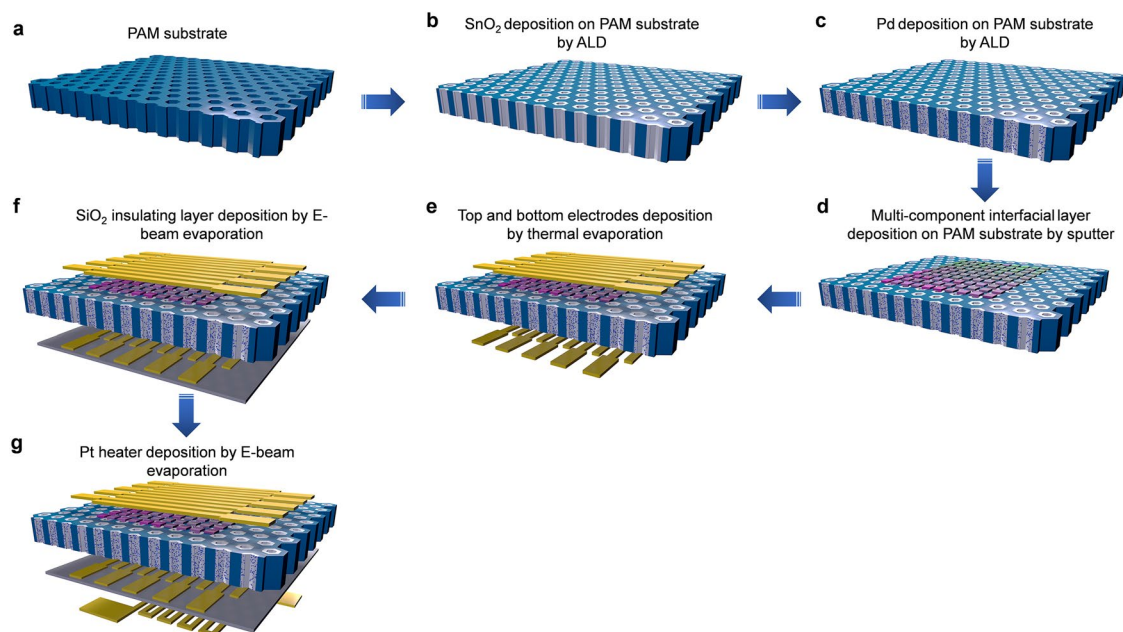
Peer review information *Nature Electronics* thanks the anonymous reviewer(s) for their contribution to the peer review of this work.

Reprints and permissions information is available at www.nature.com/reprints.

Publisher's note Springer Nature remains neutral with regard to jurisdictional claims in published maps and institutional affiliations.

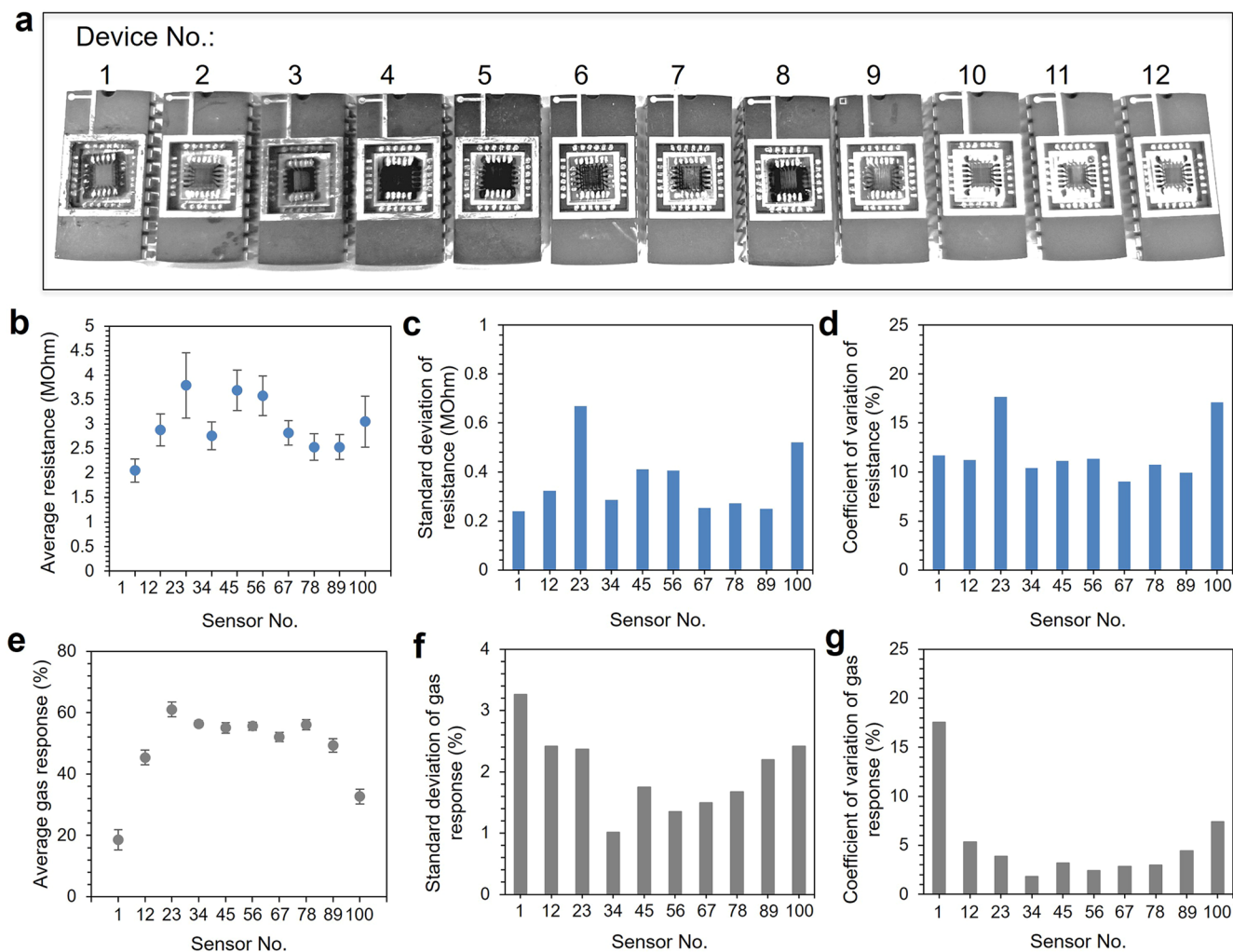
Springer Nature or its licensor (e.g. a society or other partner) holds exclusive rights to this article under a publishing agreement with the author(s) or other rightsholder(s); author self-archiving of the accepted manuscript version of this article is solely governed by the terms of such publishing agreement and applicable law.

© The Author(s), under exclusive licence to Springer Nature Limited 2024



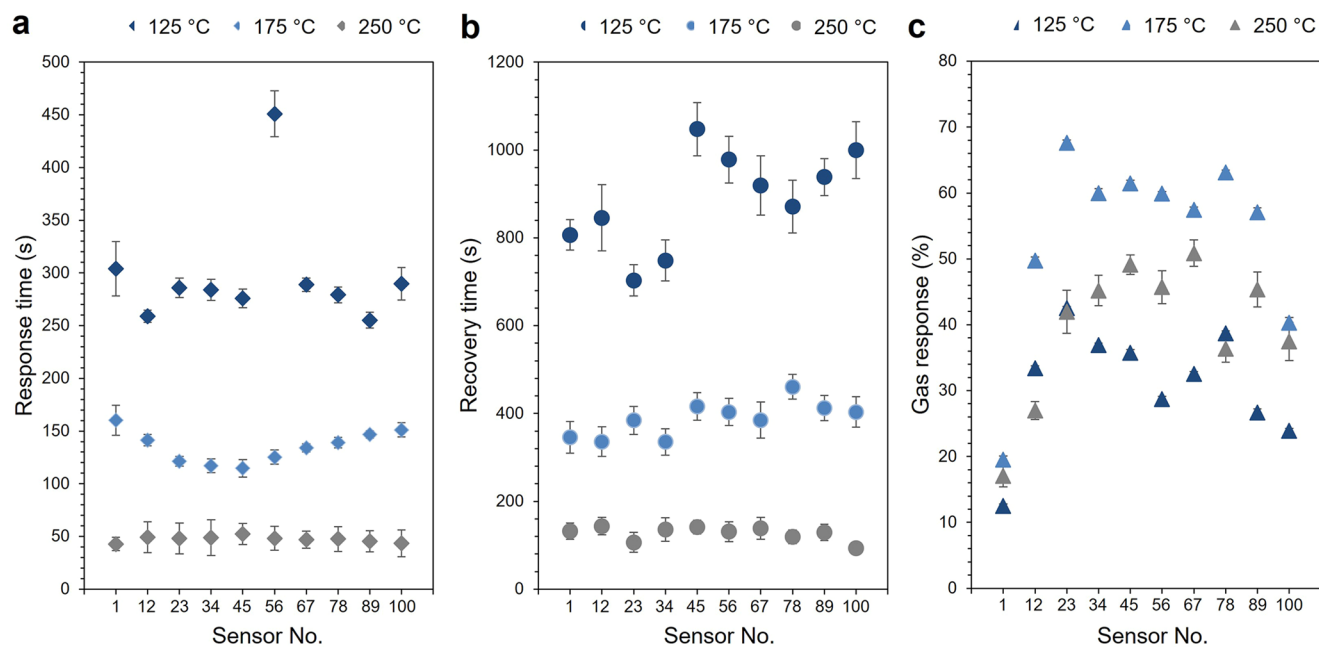
Extended Data Fig. 1 | Fabrication process of the biomimetic olfactory chip (BOC). **a**, Bare PAM substrate. **b**, SnO₂ deposition inside PAM by ALD. **c**, Pd deposition inside PAM by ALD. **d**, Multi-component interfacial layer deposition

on PAM substrate by sputter. **e**, Top and bottom Au electrodes deposition by thermal evaporation. **f**, SiO₂ insulating layer deposition by E-beam evaporation. **g**, Pt heater deposition by E-beam evaporation.



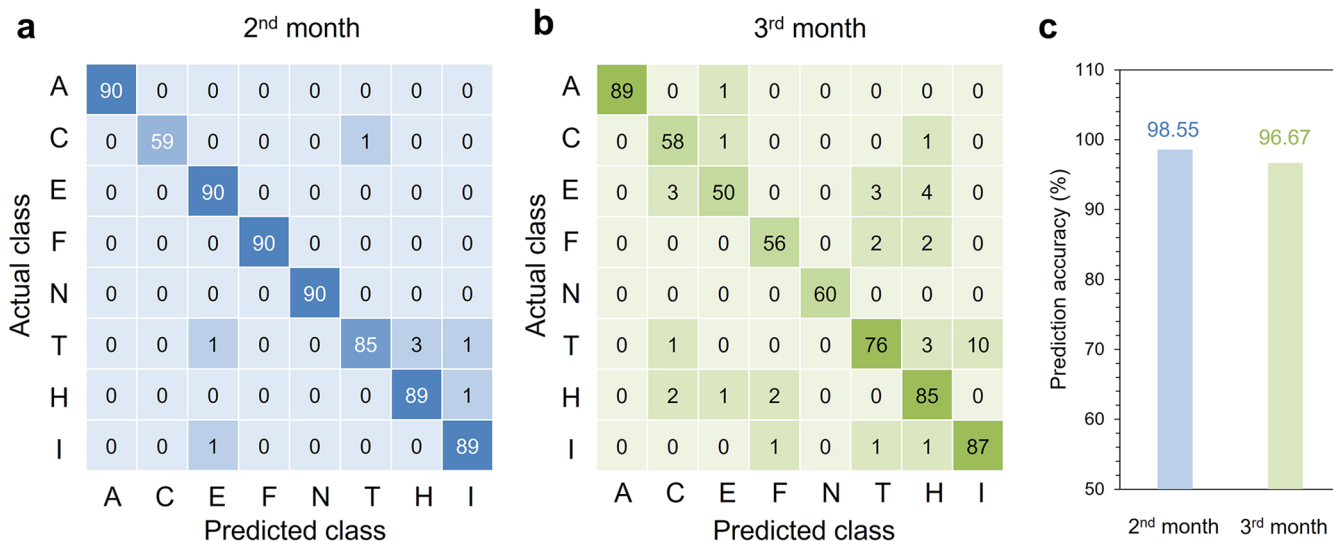
Extended Data Fig. 2 | Device-to-device repeatability test by the statistics along the diagonal sensors (Sensor #1, 12, 23, 34, 45, 56, 67, 78, 89, 100, test gas: 1 ppm acetone). **a**, Optical image of twelve 100-pixel BOC chips. **b**, Average resistance of sensors. The sample size used to derive statistics is 12. The error bars indicate the standard deviation (SD). Data are presented as mean values \pm SD.

c, Standard deviation of resistances. **d**, Coefficient of variation of resistances. **e**, Average gas response of sensors. The sample size used to derive statistics is 12. The error bars indicate the standard deviation (SD). Data are presented as mean values \pm SD. **f**, Standard deviation of gas responses. **g**, Coefficient of variation of gas responses.



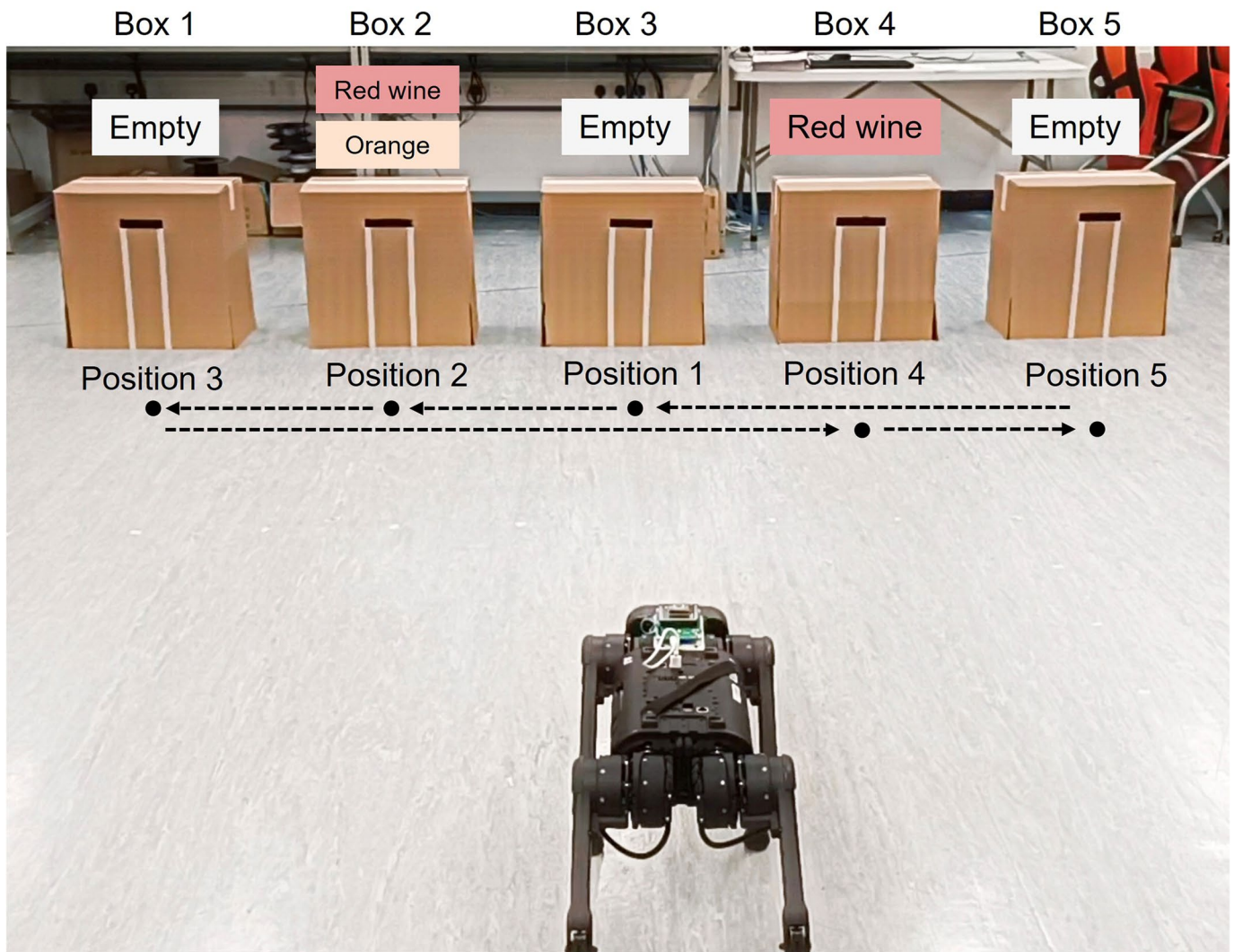
Extended Data Fig. 3 | The statistical data of the diagonal sensors' response (Sensor #1, 12, 23, 34, 45, 56, 67, 78, 89, 100) in sensor array chip to 1 ppm acetone at different working temperatures. a, Response times. b, Recovery

times. c, Gas responses. The sample size used to derive statistics is 6. The error bars indicate the standard deviation (SD). Data are presented as mean values \pm SD.

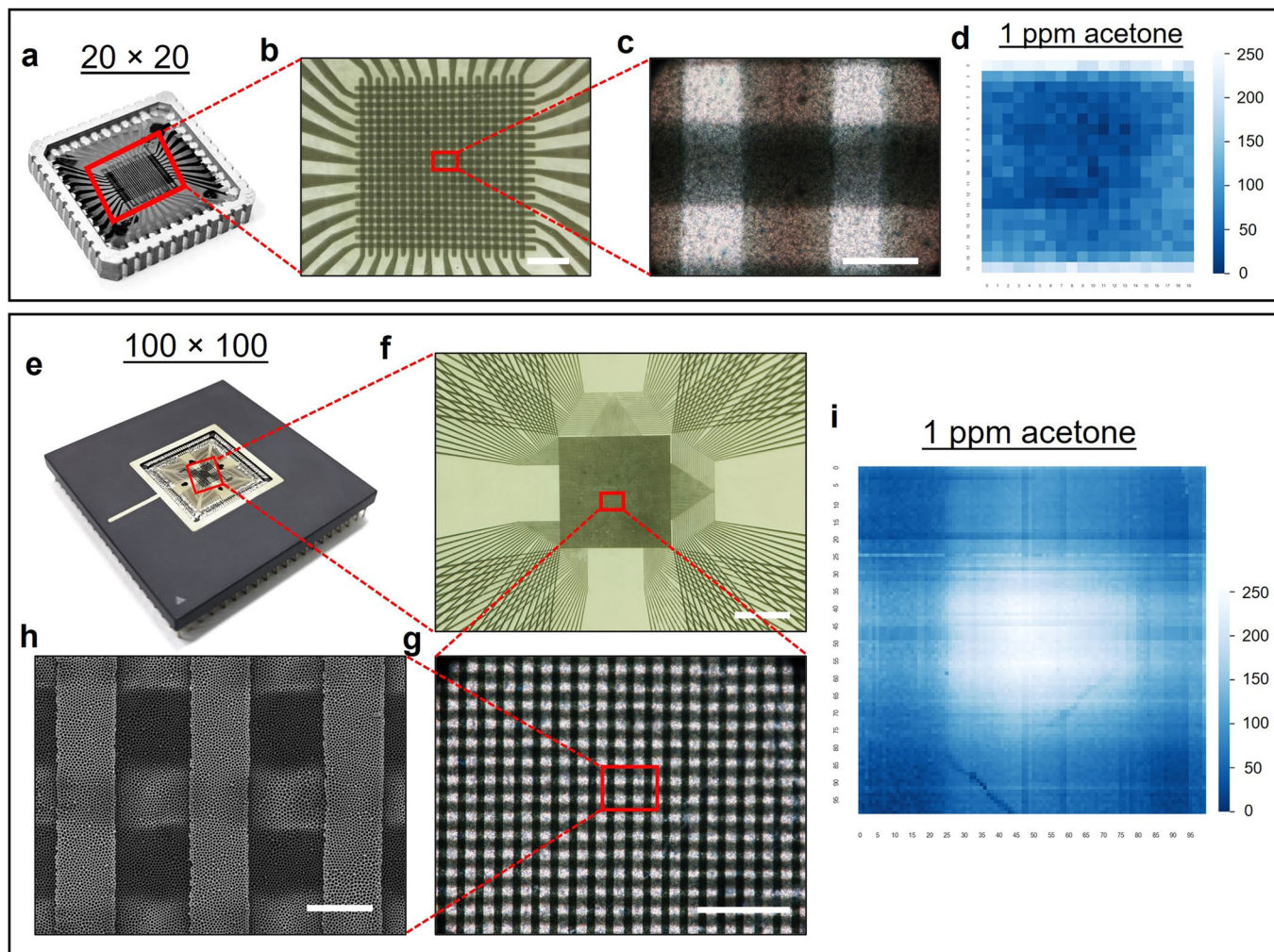


Extended Data Fig. 4 | Single gas classification with the BOC (The training data is collected in the 1st month and the test data is collected in the 2nd and 3rd months.). **a**, Confusion matrix of the actual class and predicted class for recognizing 8 gases (A: acetone, C: carbon monoxide, E: ethanol, F: formaldehyde, N: nitrogen dioxide, T: toluene, H: hydrogen, I: isobutylene) by

using the testing data collected in the 2nd month. **b**, Confusion matrix of the actual class and predicted class for recognizing 8 gases by using the testing data collected in the 3rd month. **c**, Prediction accuracy by using the 1st month data as the training data and the 2nd and 3rd months data as the testing data.



Extended Data Fig. 5 | The path design of robot for the experiment of the fusion of the quadruped robot's vision and olfactory functions to implement blind box recognition. We design two experiments: one is using only one odour (red wine), and another one is using two odours (orange and red wine).



Extended Data Fig. 6 | Construction of ultra-large-scale sensor array BOCs. **a**, Picture of 20×20 sensor array chip bonded on LCC chip carrier. **b**, **c**, Optical images of 20×20 sensor array chip with different magnification (scale bar: **b** is 1 mm and **c** is $100 \mu\text{m}$). **d**, Gas response pattern of 20×20 sensor array chip to 1 ppm acetone. **e**, Picture of 100×100 sensor array chip bonded on C-PGA chip

carrier. **f** and **g**, Optical images of 100×100 sensor array chip with different magnification (scale bar: **f** is 1 mm and **g** is $100 \mu\text{m}$). **h**, SEM image of 100×100 sensor array chip (scale bar: $10 \mu\text{m}$). **i**, Gas response pattern of 100×100 sensor array chip to 1 ppm acetone.